



# Shear failure of a granite pin traversing a sawcut fault

Gregory C. McLaskey<sup>a,\*</sup>, David A. Lockner<sup>b</sup>

<sup>a</sup> Cornell University, Ithaca, NY, United States

<sup>b</sup> US Geological Survey, 345 Middlefield Rd, Menlo Park, CA, United States

## ARTICLE INFO

### Keywords:

Moment tensor inversion  
Focal mechanism  
Asperity  
Acoustic emission  
Implosion  
Compaction

## ABSTRACT

Fault heterogeneities such as bumps, bends, and stepovers are commonly observed on natural faults, but are challenging to recreate under controlled laboratory conditions. We study deformation and microseismicity of a 76 mm-diameter Westerly granite cylinder with a sawcut fault with known frictional properties. An idealized asperity is added by emplacing a precision-ground 21 mm-diameter solid granite dowel that crosses the center of the fault at right angles. This intact granite 'pin' provides a strength contrast that resists fault slip. Upon loading to 80 MPa in a triaxial machine, we first observed a  $M -4$  slip event that ruptured the sawcut fault, slipped 40  $\mu\text{m}$ , but was halted by the granite pin. With continued loading, the pin failed in a swarm of thousands of  $M -6$  to  $M -8$  events known as acoustic emissions (AEs). Once the pin was fractured to a critical point, it permitted complete rupture events ( $M -3$ ) on the sawcut fault (stick-slip instabilities). Subsequent slip events were preceded by clusters of foreshock-like AEs, all located on the fault plane, and the spatial extent of the foreshock clusters is consistent with our estimate of a critical nucleation dimension  $h^*$ . We also identified an aseismic zone on the fault plane surrounding the fractured rock pin. A post-mortem analysis of the sample showed a thick gouge layer where the pin intersected the fault, suggesting that dilatancy of this gouge propped open the fault and prevented microseismic events in its vicinity. Recorded microseismicity separates into three categories: slip on the sawcut fault, fracture of the intact rock pin, and off-fault seismicity associated with pin-related rock joints. We found that pin fracture events were exclusively implosive (anticrack) even though the shear process zone was overall dilatant. This shows how aseismic effects can lead to unexpected seismic manifestations of certain faulting processes.

## 1. Introduction

Improvements in high speed digital data acquisition have led to increasing numbers of high quality observations of small seismic events in both laboratory and field studies. Earthquakes  $M 3$  to  $M -4$  have been used to image hydraulic fractures<sup>1,2</sup> and geothermal reservoirs,<sup>3,4</sup> study mining-induced seismicity,<sup>5,6</sup> and gain insight into the nucleation processes of larger crustal earthquakes.<sup>7,8</sup> Laboratory experiments (0.1–1 m scale), and in-situ experiments (10 m scale) conducted in underground laboratories (e.g. <sup>9</sup>) are used to study faulting processes and associated microseismicity under more idealized conditions. Such experiments can include mechanical measurements of fault slip, stresses, and forces—quantities that are largely unknown at depth—enabling a link between underlying mechanical processes and their seismic manifestations.

In laboratory rock mechanics experiments, seismic events can be broadly classified as either “stick-slip” events or acoustic emissions (AEs). Stick-slip events rupture the entire sample and are accompanied

by measureable drops in stress supported by the sample. In this paper, we refer to stick-slip events as dynamic slip events (DSEs). DSEs are thought to be analogous to earthquakes,<sup>10</sup> but their dynamics depend, at least in part, on the stiffness of the loading machine (e.g. <sup>11</sup>). AEs are smaller seismic events that are typically confined to the interior of a laboratory sample. They can be caused by microcrack formation, slip events, sudden compaction, and other mechanisms (e.g. <sup>12–14</sup>) and they are used to study the mechanics of fracture and faulting processes on the mm scale in materials ranging from rocks to reinforced concrete.<sup>15</sup> Recent progress in sensor calibration showed that AEs range from  $M -5$  down to about  $M -8$ .<sup>1,16–18</sup> While the seismic moments  $M_0$  of AEs are truly tiny, their stress drops—reflecting the events' duration relative to  $M_0$ —are consistent with scaling relationships observed for larger natural earthquakes.<sup>19,20</sup> This provides some support for a long-standing assumption that AEs can provide insight into the mechanics of larger faulting processes (e.g. <sup>21,22</sup>).

This paper presents a laboratory experiment that explores heterogeneity in a simulated fault system. A limited number of laboratory AE

\* Corresponding author.

E-mail address: [gcm8@cornell.edu](mailto:gcm8@cornell.edu) (G.C. McLaskey).

<https://doi.org/10.1016/j.ijrmms.2018.07.001>

Received 30 March 2018; Received in revised form 17 July 2018; Accepted 26 July 2018

1365-1609/ © 2018 Elsevier Ltd. All rights reserved.

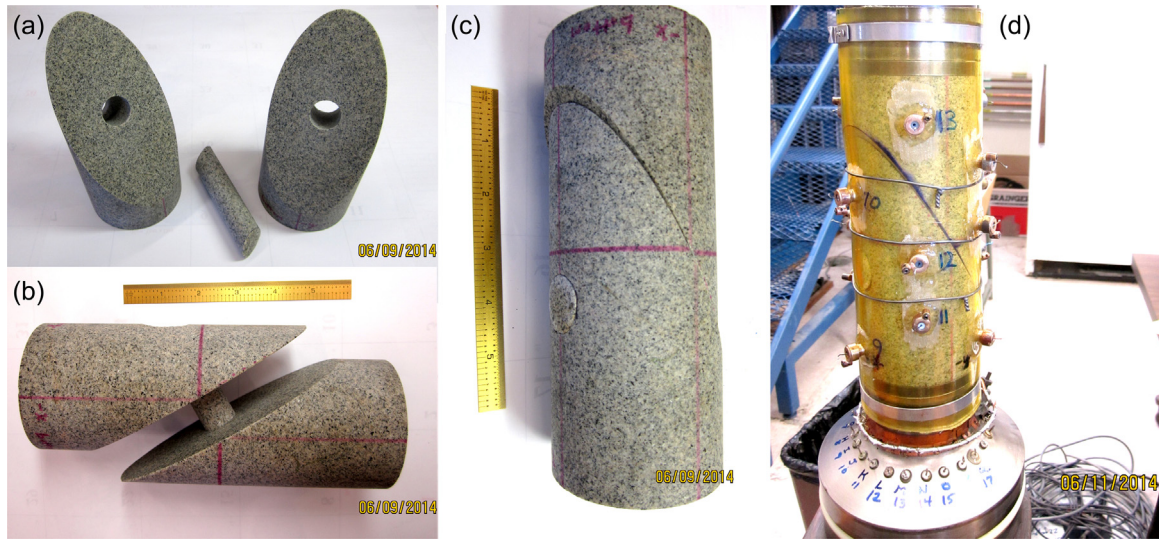


**Fig. 1.** The “pin” sample used in this study was a 76.2 mm diameter cylinder of Westerly Granite with a 30° sawcut simulated fault surface and a 20.68 mm diameter pin of intact westerly granite placed in a 20.78 mm hole oriented perpendicular to the sawcut. The sample was instrumented with an array of seventeen piezoelectric AE sensors (d) to record the locations and focal mechanisms of tiny seismic events associated with the rock deformation processes.

tests have studied deformation on ‘natural’ fault surfaces, i.e. fractured surfaces with cm-scale roughness.<sup>22–24</sup> However, rock mechanics experiments commonly employ planar faults (saw cut) that have been ground flat to simulate a more mature fault or to determine frictional properties related to mineralogy and surface contacts. Samples with saw cut faults have lower strength than intact samples, and typically initiate slip suddenly and with little warning. Using both mechanical and seismic (AE) data, studies on saw cuts have explored fault surface roughness, asperities, and the initiation and propagation of dynamic rupture,<sup>24–27</sup> but they lack variation in local shear strength due to macroscopic fault irregularities (jogs, bends, stepovers or branches) or along-strike variations in lithology and pre-stress. (Note, an early study did, in fact, observe contained rupture on a 2 m fault that had large-scale heterogeneous pre-stress.<sup>28</sup>) This is a class of fault heterogeneity that is difficult to achieve with a triaxial experiment ( $\sim 80$  MPa) where sample size is limited.

Our sample was designed to include an idealized asperity embedded in an otherwise standard laboratory sawcut fault. The asperity is a central pin of intact rock, as shown in Fig. 1. The pin makes up about 4% of the total fault surface area and provides a shear strength contrast of more than a factor of 2. We directly compared the results to our previous work on an identical sample without a pin.<sup>26</sup> We used the pin sample to test whether a 4% asperity would stop dynamic rupture and whether the remnants of the asperity would affect subsequent ruptures. AE analysis was used to explore the seismic manifestations of the above effects.

Seismic sources (both earthquakes and AEs) are typically represented with a seismic moment tensor (MT). The information contained in the MT has been used to map regional stress fields (e.g. <sup>29–31</sup>) and to discriminate between explosions, tectonic quakes, and mine collapse events (e.g. <sup>32,33</sup>) including for verification of nuclear test ban treaties.<sup>34</sup> While MT studies are routine for great earthquakes and temblors large enough to be recorded by an array of stations with wide azimuthal coverage, they are less common for microseismicity. The potential of MT analysis of AE data has long been known, but uncertainties associated with velocity models, sensor response, and low signal-to-noise ratio muddy results. It is typically unknown whether the scatter commonly observed in MT-based results is due to limited accuracy of MT solutions or if it reflects true variation in source properties. In our experiments, the locations and orientations of the pin and fault were prescribed, and different event types could be cleanly separated in time and space, so we are able to test the validity of MT

solutions on the mm scale.

When loaded, our pin sample produced a variety of types of AEs including predominantly double-couple, foreshock-like events associated with slip on the sawcut fault and other events associated with fracture of the intact granite pin. When sheared, the pin did not rupture as a single event. It failed as a swarm of thousands of AEs. On the whole, this shear process zone experienced dilatancy, and a thick layer of fault gouge was developed. Remarkably, all associated AEs had clear compaction (implosive) mechanisms indicating that dilative processes were aseismic.

## 2. Experimental procedure

Tests were performed on a cylinder of room-dry Westerly granite that was 76.2 mm in diameter and 175 mm long, as shown in Fig. 1. The sample contained a saw cut simulated fault inclined at 30° to the vertical axis and a 20.68 mm diameter cylinder of intact Westerly granite placed in a 20.78 mm diameter hole that intersected the fault at a 90° angle. The sample was jacketed in a 4.5 mm-thick polyurethane sleeve, and an array of 17 piezoelectric AE sensors (6.35 mm diameter) were separated from the rock surface by 1 mm brass fixtures. These fixtures had curved surfaces that were machined to match the sample curvature and were glued directly to the rock (Fig. 1d). The sample was then placed in a pressure vessel of a triaxial deformation apparatus and loaded at constant confining pressure  $p_c = \sigma_2 = \sigma_3 = 80$  MPa. As depicted in Fig. 2a, axial stress  $\sigma_1$  was applied with a hydraulic ram that advanced a steel piston against the bottom of the sample column. The diameter of the granite pin was precision ground to provide a close but non-interference fit inside its hole, with a clearance of approximately 100  $\mu\text{m}$ . The pin was assembled in the sample without using cement or glue that might inadvertently change the rock properties in the vicinity of the fault. Based on simple finite element models, we expected confining pressure  $p_c = 80$  MPa to elastically reduce the hole diameter by about 60  $\mu\text{m}$ . Due to its orientation, it is likely that the hole was also distorted, and this provided a modest clamping force on the pin. Axial displacement,  $z_{LP}$ , axial stress  $\sigma_1$ , and  $p_c$  were measured outside the pressure vessel and recorded continuously at 1 Hz sampling rate. The parameters  $p_c$  and  $z_{LP}$  were computer controlled using servo valves, and we imposed a constant axial shortening rate  $d(z_{LP})/dt = 5 \mu\text{m/s}$ . The total area  $A_T$  of the sawcut, including the circular cross-section of the pin, is 9122 mm<sup>2</sup>. The cross-sectional area of the pin  $A_{pin} = 336 \text{ mm}^2$ , or 3.7% of the fault area. Shear stress ( $\tau$ ) and normal stress ( $\sigma_n$ ) resolved

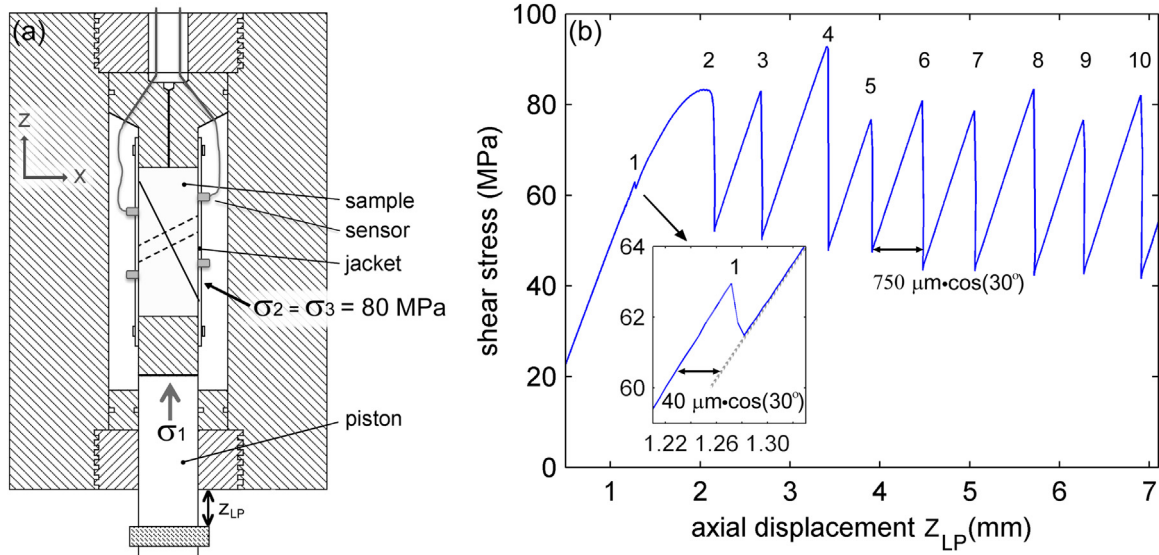


**Fig. 2.** (a) Schematic diagram of the sample in the pressure vessel of a triaxial loading apparatus. (b) Average shear stress resolved on the sawcut fault (assuming combined shear force divided by combined area of fault + pin) is plotted against load point displacement  $z_{LP}$ . Dynamic slip events (DSEs) are numbered and characterized by a sudden drop in the load supported by the sample.

on the inclined sawcut surface are reported as average stresses over  $A_T$  and are computed for a sawcut inclined at an angle  $\theta = 30^\circ$  according to:<sup>52</sup>

$$\tau = \frac{1}{2} \sigma_\Delta \sin(2\theta) \quad (1)$$

$$\sigma_n = p_c + \frac{1}{2} \sigma_\Delta [1 - \cos(2\theta)] \quad (2)$$

$$\sigma_\Delta = \sigma_1 - p_c \quad (3)$$

As slip on the fault surface accumulates, the contact area on the fault decreases, and this effect was accounted for in reporting stresses. In some cases, we report coefficient of friction which is the ratio  $\mu = \tau / \sigma_n$ . Stresses supported by the pin are not measured directly and can be significantly different from local stresses on the fault surface.

Loading at a constant  $d(z_{LP})/dt = 5 \mu\text{m/s}$  produced a sequence of 10 DSEs numbered in Fig. 2b. Signals from the seventeen piezoelectric sensors (PZ1-PZ17) were digitized (14 bit, 10 MHz) without pre-amplification or filtering, and 400- $\mu\text{s}$ -long blocks of high-speed data were recorded in a triggered mode that permitted continuous recording as long as the triggering criterion was continuously met. Eight of the seventeen channels were split and one copy of the signal was passed through a voltage divider that attenuated the signals before digitization. This allowed us to record, on scale, the large amplitude surface displacements associated with the large DSEs on eight channels while also recording the output from all seventeen sensors at high resolution for AE analysis. The eight channels that were split were chosen to have good coverage of the focal sphere for magnitude estimation described in Section 3.2.

### 2.1. Source locations

After eliminating electrical noise and other spurious events, we studied 2662 blocks of triggered data that contained at least one AE. A total of 2541 AE events were located (> 95%). About 85% of the located AEs were associated with the initial fracture of the pin and are shown in Fig. 3. The remaining 15% were associated with slip on the sawcut fault prior to DSEs 3–10, as shown in Fig. 4.

AE source locations were determined from standard inversion of P wave arrival times<sup>35</sup> in a semi-automated method where arrival times were first picked automatically and then double-checked or adjusted by hand. We used a minimum of seven sensors to compute source locations, but 95% of the AEs were located with arrival time estimates from

at least twelve sensors. We assumed the P wave velocity was 6380 m/s and 5800 m/s in the fast ( $z$ ) and slow ( $x$  and  $y$ ) directions, respectively, consistent with the  $\sim 10\%$  stress-induced velocity anisotropy previously observed in Westerly granite at similar stress conditions.<sup>26,36</sup> Deformation occurred on the sawcut fault at stress levels significantly below those required to fracture intact Westerly granite. We expected little damage or velocity change throughout most of the sample, so the velocity model used to locate events was the same for the entire experiment. Some events could not be located due to an inability to accurately pick the P wave arrival at enough sensors. This condition primarily occurred because of increased noise from reflections and reverberations (i.e. coda) either in the 150 ms after a DSE or during the crescendo of AEs that occurred just before DSE2 (Fig. 3a).

### 2.2. Uncertainty in source location

Precision of the P wave picks was 1  $\mu\text{s}$ . To estimate the uncertainty in source locations, we removed one sensor's P wave pick at random from the inversion and added to the rest of the picks a random picking error that was a uniformly distributed random number between  $-0.5 \mu\text{s}$  and  $0.5 \mu\text{s}$ . We then recalculated the source location 50 times with this random noise added and took  $\pm$  two standard deviations to estimate a  $\sim 95\%$  confidence region for source locations. Using this technique, we estimate that events near the center of the sample have  $\pm 3 \text{ mm}$  location uncertainty while events further from the center have  $\pm 6 \text{ mm}$  location uncertainty. Additional errors due to inappropriate velocity model cause a systematic bias to the locations. This is the likely cause of systematic drift of event locations off of the sawcut fault as seen in Fig. 4b. Given a near-field array of seventeen stations that surround the sample volume, a more sophisticated inversion routine that employed, for example, stress-dependent velocity anisotropy and velocity heterogeneity, would likely produce more precise event locations. However, the present location scheme provides sufficient accuracy for this analysis.

## 3. Results

### 3.1. Categories of AEs

We classified AE events into three categories based on their locations and timing. Category 1 events (light blue circles in Fig. 4) are



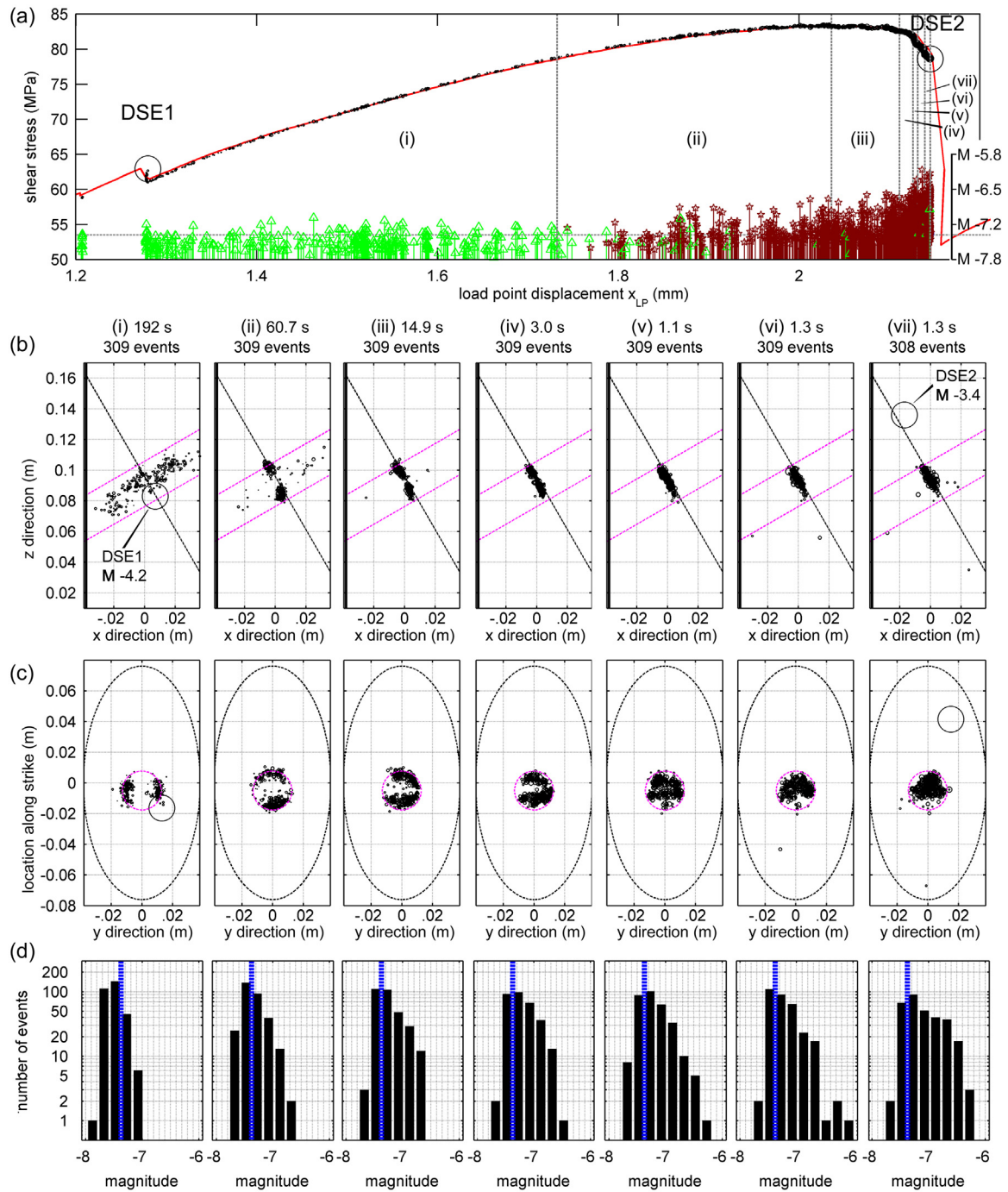


**Fig. 3.** Evolution of AE locations and magnitudes while breaking the rock pin. The sequence is divided into time periods (i)–(vii), with time durations of each period labeled, each with about 309 located AEs, 2162 total. (a) AE magnitudes and timing are plotted against the load-displacement curve. Symbols at the bottom show the AE magnitude (right y axis). Red stars are AEs associated with fracture of the intact pin and green triangles are off fault rock joint events (see text). (b) AE locations are shown in side view and (c) a projection on the fault plane. The sawcut fault is shown by a black dotted line and the outline of the rock pin is shown by magenta dotted lines. Histograms (d) of event magnitudes show how the number of larger AEs increased relative to the number of small AEs. Completeness level is shown as the vertical blue dotted line. (For interpretation of the references to color in this figure legend, the reader is referred to the web version of this article.).

those associated with slip on the sawcut fault. AEs in this category were located within 12 mm of the fault and outside of a 25 mm radius circle centered on the rock pin. Since all of these events occurred after the initial rapid surface evolution, we classify these events as resulting from slip on a “mature” fault surface. Category 2 events (dark red stars in Figs. 3 and 4) are associated with fracture of the rock pin. AEs in this category are located within 9 mm of the fault plane, inside a 25 mm radius circle centered on the pin, and occurred after phase (i) of the loading shown in Fig. 3. Category 3 events (green triangles) include all

other located events. They were primarily located on the interface between the pin and the solid sample and are hereafter referred to as rock joint events. They appear to primarily result from realignment of the inclined pin during initial sample loading, but also occurred occasionally throughout the stick-slip cycle.

### 3.2. Magnitude calculations and seismic spectra

The absolute magnitudes of AEs are rarely known. Instead relative

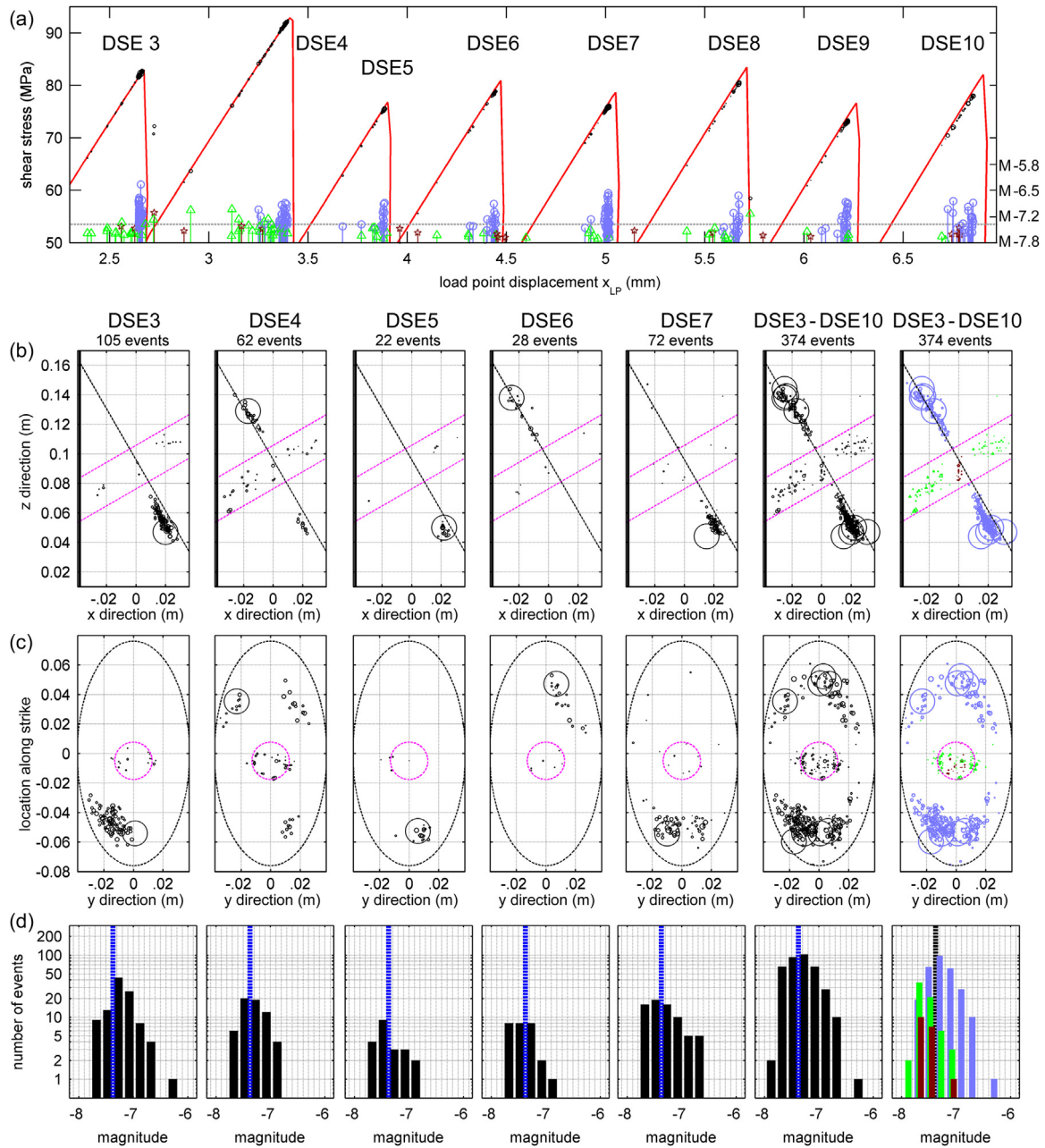


**Fig. 4.** Evolution of locations and magnitudes of AEs during the stick-slip cycle. AEs are categorized as either: (1) slip on the sawcut fault (light blue circles), (2) fracture of the intact rock pin (dark red stars), and (3) rock joint events (green triangles). (a) AEs are plotted on top the load-displacement curve showing their timing and magnitudes (right y axis) throughout the stick-slip cycle. (b) AE locations are shown in side view and (c) a projection on the fault plane. (d) Histogram of event magnitudes. Completeness level is shown as the vertical dotted line. The far right panels show locations and magnitudes colored by event type. (For interpretation of the references to color in this figure legend, the reader is referred to the web version of this article.).

amplitudes  $A_0$  are typically computed based on the maximum amplitude of recorded signals scaled for geometrical spreading at a distance of 10 mm.<sup>13</sup>

$$A_0 = \sqrt{\frac{1}{k} \sum_{i=1}^k \left( \frac{A_i r_i}{10} \right)^2}, \quad (4)$$

where  $A_i$  is the maximum signal amplitude and  $r_i$  is the source to sensor distance (in mm) for the  $i$ th of  $k$  sensors.

The absolute magnitude of a seismic source is related to the seismic moment  $M_0$  and does not depend on sensor or recording parameters.  $M_0$  can be estimated based on time domain estimates of  $\Omega_i$  (described in Section 5) or from the low frequency amplitude  $\Omega_0$  of the spectrum of the radiated waves (described below). Magnitudes of the DSEs were

derived from the source spectra, as illustrated in Fig. 5. Magnitudes of the AEs were determined from an empirical relationship,  $M_0 = \alpha A_0$ , where  $\alpha = 0.22 \text{ Nm/V}$ . This relationship holds only for the current AE sensors and apparatus geometry. It was established previously<sup>26</sup> for the same experimental setup and was double checked for a few representative AEs from this study.

The displacement source spectrum of a seismic event is the Fourier transform of recorded ground displacements with instrument response and wave propagation effects removed. It is typically constant and equal to  $\Omega_0$  at frequencies below the corner frequency  $f_0$ . Above  $f_0$ , the source spectrum has been shown to decrease approximately as  $f^{-2}$  (e.g. 37,38), where  $f$  is frequency, and  $f_0 \approx 1/T$ , and  $T$  is the time duration of the seismic source. We estimated the source spectra of AEs and DSEs by

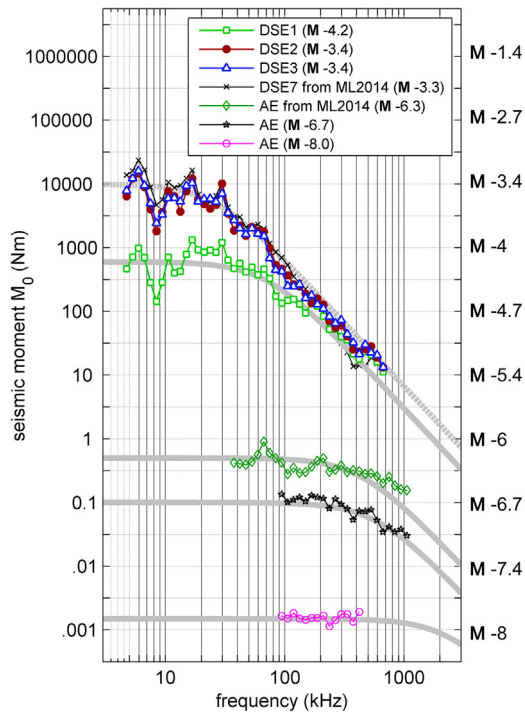


**Fig. 5.** Source spectra from the largest ( $M -3.3$ ) to the smallest ( $M -8$ ) seismic events recorded. Light gray curves show Brune spectra roughly fit to the observed data. Comparison between DSE1 and the other DSEs shows that differences in  $M_0$  are consistent with different slip amounts as estimated from mechanical data.

dividing the Fourier transform of recorded waveforms by the spectrum of an empirical calibration source with a flat displacement source spectrum. This procedure is essentially the same as the empirical Green's function technique used for analyzing earthquakes; it removes the instrument and wave propagation effects from spectral estimates.<sup>19,39</sup> For  $80 \text{ kHz} < f < 1 \text{ MHz}$ , we used a small AE with  $f_0 > 1 \text{ MHz}$  as the calibration source. For lower frequencies, small AEs have poor signal-to-noise ratio, and we used a ball impact as the calibration source. We then determined  $\Omega_0$  of a seismic event by comparing it to  $\Omega_0$  of the ball impact source that has known change in momentum.<sup>19</sup>  $\Omega_0$  is always calculated from the average of at least eight different sensors so that the radiation pattern does not bias estimates. All Fourier transforms were obtained from time windows centered on the first wave arrival and tapered with a Blackman-Harris window.<sup>40</sup> We used 20 ms duration windows for DSE spectral estimates. This long window encompasses the entire DSE source duration and is necessary to provide stable spectral estimates down to 4.5 kHz. The long windows were possible only for DSEs because their “coda” of reflections and reverberations triggered our AE system tens of times with no dead time between data blocks. AEs triggered our recording system only once, providing 300- $\mu\text{s}$  duration windows of continuous data, making spectral estimates stable down to about 90 kHz.

Source spectra for four DSEs and three representative AEs are shown in Fig. 5. They are shown only in the frequency band where there is good signal-to-noise ratio. The amplitude  $\Omega_0$  at  $f < f_0$  provides an estimate of the  $M_0$  (left axis), and we used the Hanks and Kanamori<sup>41</sup> relation to convert this to magnitude (right axis). Theoretical source spectra derived from the Brune<sup>42</sup> model are also shown in light gray.

#### 4. Interpretation AE of locations and loading curves

##### 4.1. Initial aseismic creep and strain hardening

When first loaded, the sawcut fault in our experiments sustained

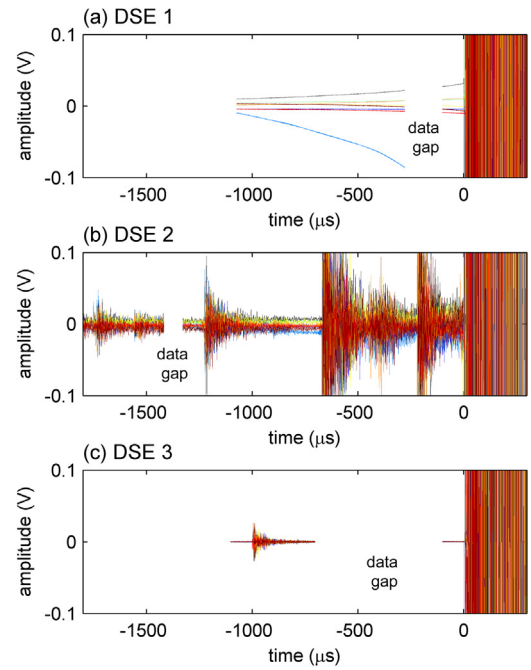


**Fig. 6.** Piezoelectric sensor data recorded immediately prior to DSE1, DSE2, and DSE3 showing premonitory activity. Time  $t = 0$  denotes the time of the DSE hypocenter. (a) DSE 1 slipped 40 mm on the sawcut fault that was halted by the intact pin. DSE 1 was preceded by a strong and accelerating, 1-ms-duration, low frequency signal interpreted as quasistatic deformation of the rock sample due to rapidly accelerating slip on the fault plane. DSE 2 occurred when the rock pin finally broke. It was preceded by a crescendo of AEs. DSE 3 through DSE 10 were more typical stick-slip events on the saw cut simulated fault preceded by a few tens of AEs. Data gaps occur when signal is too low on all channels to trigger the digitizer.

creep and strain hardened. An initial period of strain hardening is common in gouge layer experiments, but is also observed on sawcut surfaces (see, for example<sup>43</sup>). This process is related to crushing of the highly stressed grain contacts (approximately 15  $\mu\text{m}$  surface roughness in this experiment).<sup>44</sup> As the contacts are crushed, shear stress is distributed more uniformly, the sample supports increasing stress and becomes more unstable and seismogenic. In the current experiment, no AEs were detected on the sawcut until after DSE2 and  $> 1 \text{ mm}$  of cumulative slip. In a previous study, foreshocks were also not observed on the sawcut fault until after the first DSE and  $> 1 \text{ mm}$  of cumulative slip had occurred (see Fig. 2b and Fig. 9d of<sup>26</sup>). After this initial rapid surface evolution, strain hardening was minimal and subsequent stick-slip cycles (DSEs 3–10) showed very little creep or inelastic behavior.

##### 4.2. DSE1–Dynamic slip halted by the intact pin

When the sample was first loaded, a relatively small instability occurred, which we refer to as DSE1 ( $M -4.2$ ,  $\mu = 0.54$ ,  $\tau \sim 63 \text{ MPa}$ , see Fig. 2). DSE1 initiated differently from all other DSEs. It lacked foreshocks, and, as shown in Fig. 6a, low frequency ground motions were detected by the piezoelectric sensors in the final 1 ms before DSE1. The piezoelectric sensors are primarily sensitive to acceleration in this  $< 1 \text{ kHz}$  frequency band, and the motions they detected were likely caused by rapidly accelerating aseismic slip on the sawcut. This acceleration of fault slip must have occurred only in the final fraction of a second before DSE1, since no anomalous fault slip could be determined from 1 Hz mechanical data, as shown in Fig. 7. The accelerating aseismic slip abruptly turned seismic with distinct P-wave arrivals. The hypocenter was located near the intersection of the pin and the sawcut fault. Similar low frequency piezoelectric sensor recordings have been detected during the nucleation of DSEs on a 2-meter fault experiment



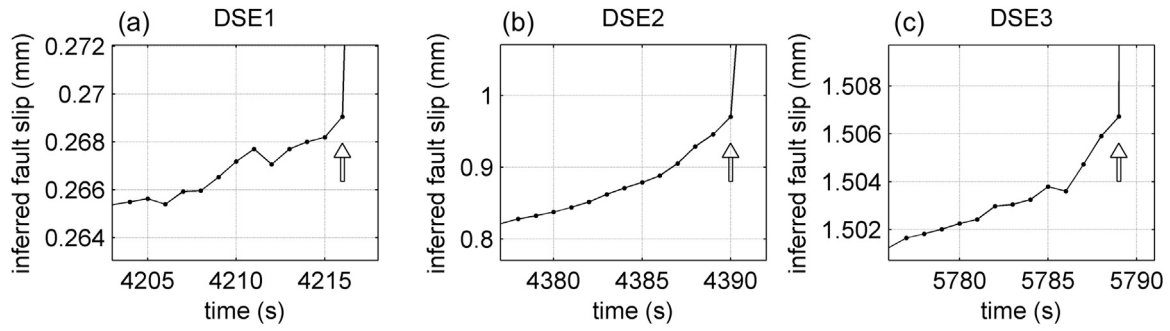


**Fig. 7.** Inferred fault slip in the seconds preceding DSE1, DSE2, and DSE3. Note that the amplitude scale is different in (b) since fault slip rates are much higher ( $\sim 15$  mm/s) prior to DSE2 than other DSEs ( $\sim 0.5$  mm/s). Data were collected at 1 Hz and individual data points are shown. The arrow indicates the last 1 Hz data point before the DSE. We estimated fault slip  $d$  on the sawcut fault from mechanical data  $d = (z_{LP} - t/k)/\cos(30^\circ)$  where  $k$  is the stiffness of the sample and loading column.  $k \sim 60$  GPa/m was estimated by assuming fault slip rate is zero for the initial loading at low  $t$ . In some instances the signals appear to decrease, but this is likely due to the  $\sim 1$ – $2$  mm of noise in the data and does not imply that the fault slipped backwards.

conducted at 5 MPa stress levels,<sup>45</sup> but they are absent from the nucleation of all other DSEs in the current experiment (Fig. 6). We note that most AE recording systems are blind to such low frequency piezoelectric signals ( $< 500$  Hz) because they are far below the frequency band of most AE preamps. In the current study, they were only detected on the nine channels that were directly connected to our high input impedance digitizer without the use of preamps or attenuators, so they would not have been detected in our previous study.<sup>26</sup>

We estimate that DSE1 was the result of  $40 \mu\text{m}$  of slip that occurred approximately uniformly across the entire sawcut fault and was arrested by the intact rock pin. The slip amount was estimated from the loading curve (Fig. 2b inset). The source spectra of the radiated seismic waves, shown in Fig. 5 provide additional support for this interpretation. The ratio between the slip during DSE1 ( $d_1 = 40 \mu\text{m}$ ) to the slip during subsequent DSEs ( $d_2 \approx d_3 \approx d_6 \approx d_7 \approx 750 \mu\text{m}$ ) is the same as the ratio of their seismic moments estimated from their spectra:

$$d_1/d_7 = 40 \mu\text{m}/750 \mu\text{m} \approx M_{\text{DSE1}}/M_{\text{DSE7}} = 600 \text{ N m}/10000 \text{ N m} \quad (5)$$

Seismic moment is  $M_0 = GA d$ , where  $A$  is the fault area,  $d$  is slip, and  $G$  is a stiffness parameter with units of stress. For earthquakes,  $G$  is equal to the shear modulus of the rock mass, but for laboratory generated DSEs  $G$  may depend on the loading apparatus (e.g.<sup>11</sup>). Eq. (5) indicates that mechanically derived slip estimates are consistent with the seismically derived slip estimates and that the quantity  $GA$  is consistent between DSE1 and other DSEs, supporting our interpretation that DSE1 involved slip across the entire sawcut fault. How did an average of  $40 \mu\text{m}$  of slip accumulate on the fault without fracturing the rock pin? As stated in Section 2, the pin was designed to provide an initial clearance of  $\sim 100 \mu\text{m}$ , approximately 60% of which was likely eliminated by elastic closure of the surrounding hole by application of confining pressure. We interpret the initial  $180 \mu\text{m}$  of creep and  $40 \mu\text{m}$  coseismic fault slip during DSE1 as fault slip needed to pre-load the pin to incipient failure. Continued loading produced additional fault creep that quasistatically fractured the rock pin, culminating in DSE2.

No Omori-type aftershock sequences were observed for most DSEs. This is likely because DSEs rupture the entire sample and the fault is macroscopically flat, so there are no stress concentrations within or at the edges of the rupture area. However, DSE1 produced tens of aftershocks with approximate  $1/t$  decay in the numbers detected for the first few seconds following after DSE1. These aftershocks were located on the sides of the pin as shown in Fig. 3(i).

#### 4.3. DSE2 was delayed until the pin was sheared quasistatically

Following DSE1, creep of the sawcut continued to load the intact rock pin, and as stresses approached critical, thousands of AEs illuminated the shear process zone. Unique to DSE 2 was large inelastic strain and fault creep ( $660 \mu\text{m}$ ) that preceded the instability (Figs. 2b, 3a, and

7b). Immediately after DSE1, AEs occurred all along the sides of the pin where it was presumably rubbing against the inside of its hole (Fig. 3i). AE locations then moved to the intersection of the pin and the sawcut fault, first at the leading and trailing edges of the pin (Fig. 3ii) where it was loaded by the creeping fault. As the sample reached peak shear stress and then steadily weakened, AE events progressed from the perimeter of the pin towards its center (Fig. 3iii–vi). We interpret this migration of AE locations as the result of two fracture fronts that progressed from opposite sides of the pin towards its center as it was quasistatically sheared by loading from the sawcut. A similar progression of AE locations has been reported for nucleation and growth of fracture fronts in intact granite samples loaded to failure.<sup>46–51</sup> It is unlikely that the observed migration in AE locations is an artifact of increasing damage in the sample since that damage is confined to a small section of the pin. The sample-averaged stress levels are far below those required to fracture intact rock, so the majority of the sample was undamaged.

Shear stress supported by the sample peaked and then decreased by 4.1 MPa before the onset of DSE2. Accelerating creep of the fault (Fig. 7b) and accelerated destruction of the granite pin in the final seconds before DSE 2 produced a crescendo of hundreds of AEs of increasing amplitude and culminated in DSE2. Only 2 AEs (out of 2162) were detected on the sawcut fault during this loading phase. The DSE2 hypocenter was located on the sawcut about 40 mm from the pin, shown in Fig. 3vii. Tens of aftershocks were observed (not shown), though these events were difficult to analyze amid the "coda" of vibrations that ensued for 150 ms.

We initially hypothesized that the DSE that fractured the pin would exhibit anomalous seismic signatures, but this was not the case. We studied both waveforms and spectra of the DSEs but found nothing remarkable about DSE2. The source spectrum of the radiated waves from DSE2 was no different from the spectra of later DSEs, as shown in Fig. 5. One might also expect DSE2 to radiate high frequency seismic waves more intensely than other DSEs due to comminution of the newly fractured pin. Fig. 8 shows how DSE spectral levels changed throughout the sequence of 10 DSEs. There is a weak trend of decreasing high frequency radiation (350–700 kHz) with increasing DSE number, as the simulated fault was progressively worn, but DSE2 was not anomalous.

The 4.1 MPa quasistatic drop in shear stress supported by the sample between peak stress ( $\tau_{\text{peak}} = 83.3$  MPa) and the onset of DSE2 represents a 5.2% drop in overall strength. This is consistent with the strength loss expected for the granite pin transitioning from intact strength to frictional sliding strength. To show this, we estimate intact rock strength  $\sigma_1 = 748$  MPa of westerly granite from Eq. (6) of<sup>52</sup> assuming  $\sigma_3 = p_c = 80$  MPa. Then, from Eq. (1), peak shear stress supported by the pin is  $\tau_{\text{intact}} = 289$  MPa. Next we assume granite friction  $\mu = 0.7$  for the fractured pin. Again, using Eq. (1) we determine  $\sigma_1 \approx 297$  MPa and  $\tau_{\text{friction}} \approx 94$  MPa for stresses supported by the

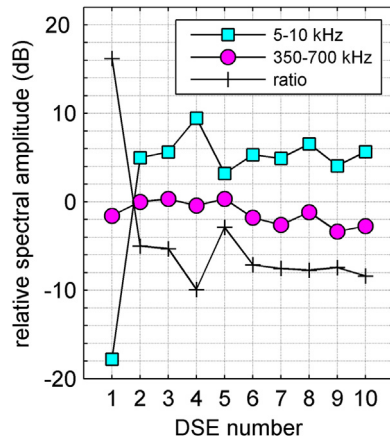


**Fig. 8.** Changes in DSE spectral levels throughout the experiment. The amplitudes at frequencies below  $f_0$  (5–10 kHz) are very well correlated with the drops in shear stress shown in Fig. 2b, because both  $W_0$  and drops in shear stress are proportional to slip on the sawcut. High frequency spectral levels (350–700 kHz) show a gradual decrease with continued wear of the sawcut. This trend is largely independent of the overall size of the DSE, as shown by the ratio (350–700 kHz / 5–10 kHz).

sheared pin after it has failed. The cross-sectional area of the pin is 3.7% of the total fault area  $A_T$  (Section 2). As seen from the AE locations in Fig. 3iii, about  $\frac{1}{2}$  of the pin had failed at the time of peak stress, so pin area at peak stress  $A_{\text{peak}} \approx (3.7\%/2)A_T$ . Then, the expected strength reduction of the sample when the pin fails is estimated as  $(1 - A_{\text{peak}})(\tau_{\text{intact}} - \tau_{\text{friction}})/(A_T \tau_{\text{peak}}) \approx 4.3\%$ . This expression simply assumes that the strength loss of the pin is weighted by its area relative to the total fault area.

The timing of DSE2 is linked to the pin fracture. If the pin had failed independently of DSE2, then total fault strength, as shown at the end of Fig. 3a should have first stabilized. Instead, fault creep and fault weakening accelerated smoothly into DSE2. This suggests that the final stage of failure of the pin involved sufficient strength loss to induce the onset of fault instability, even though DSE2 initiated on the sawcut about 40 mm or 2 diameters away from the pin and produced no anomalous seismic radiation.

#### 4.4. DSE3 through DSE10—clustered foreshock sequences

After the rock pin was sheared, DSE3–DSE10 were generated in standard stick-slip cycles. Nearly all attributes of these DSEs including their foreshocks (Category 1 AEs) and initiation were similar to those performed on a standard sawcut sample without a pin, as reported in,<sup>26</sup> except that the overall sample strength and the magnitudes of the AEs were both somewhat larger without the pin (see Table 1).

Early in the experiment (i.e. DSE3 and DSE4) some Category 2 and

**Table 1**

AE and DSE characteristics comparing the pin sample and experiments on a sawcut sample without the pin (ML2014).<sup>26</sup>

|                                    | ML2014 tests: DSE1 – DSE7                        | This paper: DSE2–10 |
|------------------------------------|--|---------------------|
| Sample Type                        | Sawcut   | Sawcut with pin     |
| Sawcut surface prep                | surface ground and lapped with 600 grit abrasive | same                |
| Confining Pressure                 | 80 MPa   | 80 MPa              |
| Peak strength (coeff. of friction) | 0.68–0.71  | 0.62–0.69           |
| Drop in shear stress during DSE    | 65–70%   | 40–50%              |
| Largest AE on Sawcut Fault         | M -5.7   | M -6.3              |

Category 3 events were recorded even at low stress levels, but Category 1 events were only recorded in the final seconds before a DSE. Remarkably reminiscent of foreshocks observed in nature (e.g. <sup>53,54</sup>), these late-stage Category 1 events were clustered on specific patches on the fault plane and often showed migration toward the eventual DSE hypocenter (largest black circle). The foreshock clusters occurred on both ends of the simulated fault, indicating that stress was near critical at many locations, but no events were located in a  $\sim 25$  mm wide annulus surrounding the pin. DSE hypocenter locations always alternated between the two ends of the simulated fault. Later in the experiment (DSE9 and DSE10), fewer category 3 events were observed and AEs on the fault plane began to occur earlier in the stick-slip cycle at lower overall stress levels (see Fig. 4a), perhaps as a result of accumulating damage of the fault surfaces.<sup>55</sup> No Omori-type aftershock sequences were observed, probably because DSEs rupture the entire sample and therefore do not leave stress concentrations near the perimeter of their ruptured areas as expected for natural earthquakes.

## 5. Focal mechanisms and moment tensor inversion

### 5.1. Background and methodology

Seismic sources that are small compared to source-sensor separation can be represented with a second-order symmetric moment tensor  $M_{pq}(t)$ .<sup>56</sup> This has six independent unknowns that are related to the focal mechanism, described below.  $M_{pq}(t)$  can be obtained from the inversion of recorded ground motions  $u_r(t) = M_{pq}(t) \otimes G_{rp,q}(t)$  where  $\otimes$  indicates convolution and  $G_{rp,q}(t)$  is the first spatial derivative of the Green's function that describes wave propagation and varies with source and sensor location and characteristics of the propagation medium.

Often in AE analysis, focal mechanisms are estimated simply from the polarity of direct P wave arrivals. If P waves can be measured by enough sensors with adequate coverage of the focal sphere, mostly compressional first arrivals indicates an explosion or an opening crack, dilatational first arrivals are interpreted as implosion, and mixed arrivals as shear-type events (e.g. <sup>24,57–60</sup>).

In this work, we inverted for the full moment tensor. We invoked the common assumption that the time history of the source  $s(t)$  is separable from its amplitude and directionality such that  $M_{pq}(t) = M_{pq}s(t)$ , and we estimated  $M_{pq}$  from amplitudes and polarities of the direct P waves using the 'focimt' script from the MATLAB-based hybridMT software package.<sup>61</sup> The main input parameters for this code are: the azimuth  $\theta_i$  and takeoff angle  $\phi_i$  of the P wave ray path  $\vec{p}_i$  that travels from the source to the  $i^{\text{th}}$  of  $N$  sensors, the angle of incidence of  $\vec{p}_i$  with respect the sensor's sensitivity vector  $\mathbf{t}_i$ , the distance  $r_i$  along the ray path from source to sensor, and  $\Omega_i$ , which is the area under the curve of the first P-wave ground displacement pulse. A homogeneous and isotropic velocity model with straight-line ray paths was assumed when calculating takeoff and incidence angles.

AE sensors are primarily sensitive to unidirectional ground motion in the poling direction of the piezoelectric crystal. In our sensor geometry, the sensors' axis of sensitivity  $\mathbf{t}_i$  is a vector that lies on the x-y plane and passes through the axis of the cylindrical sample. The amplitude measured by the sensor  $a_i = \mathbf{p}_i \cdot \mathbf{t}_i$  where  $\cdot$  denotes a dot product and  $\mathbf{p}_i$  describes P-wave amplitude along the ray path  $\vec{p}_i$ . We assumed that sensor sensitivity does not vary as a function of incidence angle or frequency. The latter was justified since a previous study showed that the voltage output from the piezoelectric sensors was roughly proportional to displacement in the approximate  $100 \text{ kHz} < f < 500 \text{ kHz}$  frequency band that dominates the AE recordings.<sup>19</sup> We substituted our estimates of  $a_i$  for  $\Omega_i$  in the hybridMT code. This substitution produces valid MT solutions (without absolute magnitude) as long as the time duration of the P-wave pulse is constant between all sensors' recordings (i.e. directivity is neglected). Observations of recorded waveforms, such



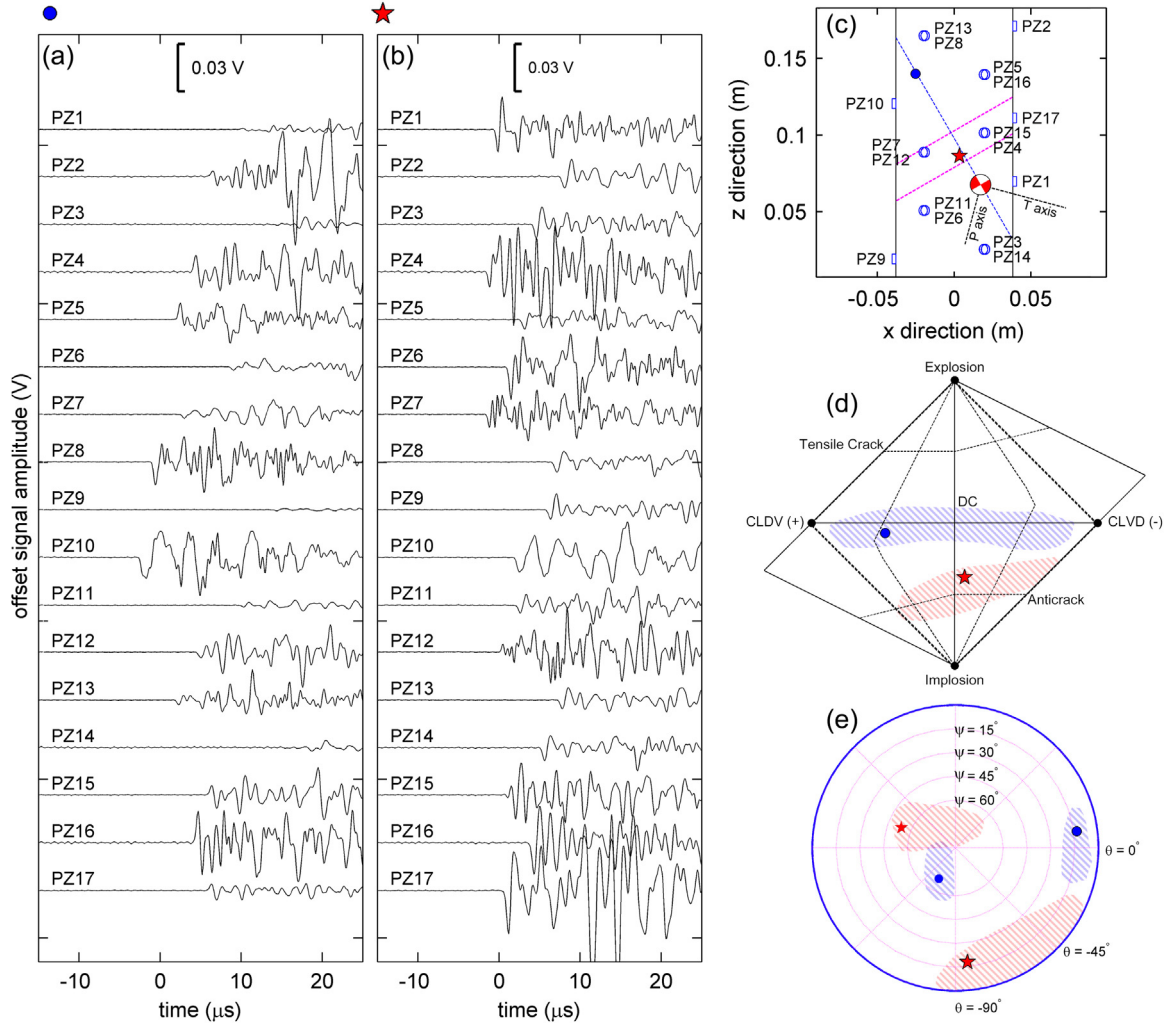


**Fig. 9.** Comparison of waveforms and focal mechanisms between a typical Category 1 event associated with slip on the sawcut fault plane and a Category 2 event associated with destruction of the rock pin. (a) and (b), Recorded signals from the seventeen AE sensors are shown on the same scale; both events are  $M_0 = 0.014$  Nm ( $M - 7.3$ ). (c) The locations of the two events are shown in relation to the sample, AE sensors, sawcut fault (blue dotted line), and the outline of the rock pin (magenta dotted line). The red and white beach ball shows the orientations of the  $P$  and  $T$  axes for a DC mechanism on the fault plane. Parameters derived from the seismic moment tensor estimated for each event are shown (d) on a Hudson plot, and (e)  $T$ -axes (larger symbol with black outline) and  $P$ -axes (smaller symbol without black outline) on the focal sphere. The hashed regions show the approximate distribution of results from other events of the same category, as shown in more detail in Fig. 10. (For interpretation of the references to color in this figure legend, the reader is referred to the web version of this article.).

as those shown in Fig. 9, confirmed that this was typically the case. Rather than utilizing the hybridMT code to calculate  $M_0$ , we derived it from spectral estimates, as described in Section 3.

The output of the hybridMT code includes all six independent components of  $M_{pq}$  as well as estimates of errors in the solution. We studied parameters  $u$  and  $v$  derived from  $M_{pq}$  which are the  $x$  and  $y$  axes of a Hudson source-type plot<sup>62</sup> as shown in Fig. 9d. The parameter  $v$  depends on the relative strength of the isotropic component of  $M_{pq}$ , while  $u$  depends on the relative strength of the compensated linear vector dipole (CLVD) and double couple (DC) components of the deviatoric portion of  $M_{pq}$ . We determined the orientations (azimuth and plunge) of the  $T$  and  $P$  axes which are the eigenvectors of the largest and smallest eigenvalues of  $M_{pq}$ , respectively. The  $P$  (compressional) and  $T$  (tensional) axes will match the maximum and minimum principal stress directions if the motion takes place on an optimally oriented fault plane. We also obtained RMS error from the hybridMT code defined:

$$RMS = \sqrt{\frac{\sum_{i=1}^N (U_i^{meas} - U_i^{th})^2}{\sum_{i=1}^N (U_i^{meas})^2}} \quad (6)$$

where  $U_i^{meas}$  is the P-wave amplitude observed at the  $i^{th}$  of  $N$  sensors,

and  $U_i^{th}$  is the expected P-wave amplitude at the  $i^{th}$  sensor based on  $M_{pq}$  determined from the moment tensor inversion.

P wave amplitudes were calculated in an automated procedure and then double checked by hand. Ambiguous amplitudes were removed from the inversion. Solutions with high RMS values were not stable, and a small change in the reported amplitudes resulted in large changes in MT results. We report only moment tensor solutions with  $N \geq 12$  and  $RMS \leq 0.40$ .

## 5.2. Focal mechanism results

Fig. 9 shows waveforms, locations, and focal mechanism results for two example events of equal magnitude and RMS errors of about 0.3. The category 1 event (light blue circle) has mixed P-wave first motions. Sensors in dilatational quadrants (all sensors below the sawcut fault plus PZ8 and PZ13) see down first motions, while sensors in compressional quadrants see up first motions. This event does not have any significant isotropic component. The category 2 event has down P-wave first motions (dilatational) on all channels except PZ12. Polarity of PZ15 is ambiguous and has nearly zero amplitude despite its close proximity to the source. This event lies near the anticrack on the

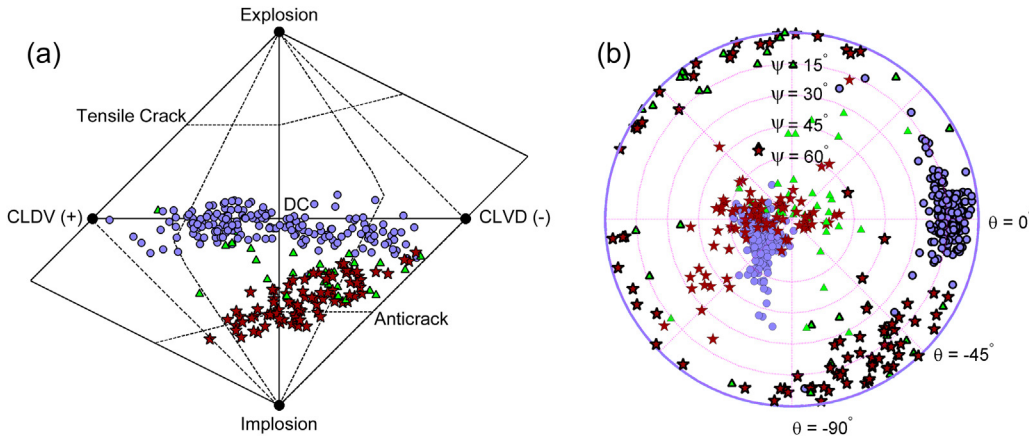


**Fig. 10.** Focal mechanism results for events generated both during the destruction of the pin and subsequent stick-slip cycles are plotted on (a) the Hudson source type plot, and (b) the orientations of the  $P$  and  $T$  axes on the focal sphere. In (b), symbols with bold black outlines show the  $T$  axis and symbols with thin outlines show the  $P$  axis. Each symbol (or pair of symbols in (b)) represents a different AE. Light blue circles are AEs located on the fault plane, dark red stars are AEs associated with the fracture of the pin, and green triangles are off-fault AEs associated with pin-related rock joints. (For interpretation of the references to color in this figure legend, the reader is referred to the web version of this article.)

Hudson source type plot and has significant implosive components.

Fig. 10 shows focal mechanism results for all events analyzed. AEs located on the fault plane (Category 1) typically had less than 15% isotropic component. Their distribution was broadly centered near DC with up to  $\pm 70\%$  CLVD, and the orientations are remarkably consistent and clustered around the expected orientations for shear slip on the sawcut fault plane:  $T$  axis  $\theta = 0$  ( $+x$  direction),  $T$  axis plunge  $\psi = 15^\circ$ ;  $P$  axis  $\theta = 180^\circ$ ,  $P$  axis  $\psi = 75^\circ$ . A beach ball with these expected  $P$  and  $T$  axis orientations is depicted in Fig. 9c. Category 2 events were exclusively implosive ( $-15$  to  $-70\%$  isotropic component) and were broadly distributed near the anticrack on the Hudson source-type plot. Orientations of Category 2 events were not as consistent as for Category 1 events, and most had  $T$  axes with  $-45^\circ < \theta < -90^\circ$ .  $\pm 90^\circ$  would suggest that  $\sigma_3$  is roughly in the direction of the  $y$  axis, as would be expected for predominantly biaxial shearing of the pin in the  $x$ - $z$  plane. The  $P$ -axis of nearly all events of Category 1 and 2 had a  $P$  axis plunge  $\psi > 60^\circ$ . ( $\psi = 90^\circ$  is the direction of applied  $\sigma_1$ .)

### 5.3. Scatter in MT results

In general, we found that the vertical axis ( $v$ ) of the Hudson source-type plot (the isotropic component) was a good discriminator of event type, but a large amount of scatter was observed in the horizontal axis ( $u$ ) on the Hudson source type plot, consistent with large  $u$  uncertainties found in previous studies (e.g. <sup>14,32</sup>). We found no significant variation in MT results as a function of magnitude, and the scatter of observed results persisted even for larger AEs.

We performed a forward sensitivity analysis to explore if the scatter in MT results is due to inaccuracy in the MT inversion or reflects true variation in the source mechanisms. To simulate reasonable levels of uncertainty in the input parameters, we (1) added  $\pm 500 \mu\text{V}$  random errors to each  $P$ -wave amplitude estimate to reflect the  $\sim 500 \mu\text{V}$  peak-to-peak noise present in the AE sensor data, (2) added  $\pm 3 \text{ mm}$  random source location errors, (3) added a more significant  $\pm 3.5 \text{ mV}$  uniformly distributed random  $P$ -wave amplitude error to one channel at random, and (4) removed one channel at random from the inversion. Random errors (1) and (2) alone were clearly not enough to match the scatter observed in Fig. 10, but when all four of these random errors were included, as shown in Fig. 11, scatter was nearly comparable to that shown in Fig. 10, at least in the horizontal axis of the Hudson source-type plot. Particularly for Category 1 events, most of the scatter observed in Fig. 10 can be the result inaccuracy of the MT inversion due to the aforementioned errors in source location and  $P$  wave amplitudes and does not represent any underlying variation in source type. All events could be nearly pure DC source mechanisms oriented on the simulated fault plane. For Category 2 events, some of the scatter in MT results shown in Fig. 10, especially in the isotropic component, is likely

due to variation in the source mechanisms, but most of the scatter in the horizontal axis of the Hudson source-type plot is likely due to inaccuracy of the MT inversion.

One additional source of error not mentioned above is velocity anisotropy and associated attenuation anisotropy.<sup>36</sup> Velocity anisotropy was neglected in the calculation of takeoff angles, and attenuation isotropy would cause lower-than-expected  $P$ -wave amplitudes for ray paths predominantly oriented in the  $x$  direction compared to ray paths predominantly oriented in the  $z$  direction.

## 6. Discussion

### 6.1. Initiation/nucleation of dynamic rupture

Laboratory rock mechanics experiments are typically conducted on either intact samples<sup>46,58,63,64</sup> or samples that contain a sawcut simulated fault.<sup>22,24,27,65</sup> Intact rock samples are stronger, and when loaded, they produce diffuse AEs that eventually localize onto a fault plane inclined approximately  $30^\circ$  from  $\sigma_1$ , the most compressive principal stress direction.<sup>46,59</sup> Initiation of the macroscopic fracture occurs by coalescence of microcrack damage in a cluster of AEs with linear dimensions of  $20$ – $40 \text{ mm}$ .<sup>46–49</sup> Since we used an asperity that is not larger than this dimension, we did not expect to see dynamic rupture initiate from within the granite pin. Given the strength contrast between intact and fractured granite ( $\sim 200 \text{ MPa}$  shear stress when at  $80 \text{ MPa}$  confining pressure), we would expect to see distinct fracture nucleation and propagation phases only for an asperity that was  $5$ – $10$  times larger, but our limited sample size prohibits us from testing this hypothesis. Instead, the accelerating AE rate and creep shown in Fig. 3ii–vii is similar to the quasistatic nucleation process observed in larger intact samples, but occurs at lower sample-average stress levels.

A different class of model predicts rupture nucleation and growth for a planar fault with uniform frictional properties (e.g. <sup>66–69</sup>). In this case, fault creep must reach a critical patch size  $h^*$ , after which rupture grows dynamically. Though precise formulations for  $h^*$  vary, we roughly estimate  $h^*$  from

$$h^* \approx \frac{GD_c}{\sigma_n(b-a)} \quad (7)$$

and assume shear modulus  $G = 30 \text{ GPa}$ , rate-state- parameter (b-a)  $\approx 0.004$  for granite, and  $D_c \approx 1 \mu\text{m}$  for the finely ground sawcut surfaces. Using these parameters and the measured  $\sigma_n \approx 130 \text{ MPa}$  provides us with  $h^* \approx 58 \text{ mm}$ . This critical patch size is remarkably similar to the linear dimensions of clusters of AEs located on the fault plane that preceded DSE3 through DSE 10, as shown in Fig. 4c. This suggests that these AE clusters are driven by localized and accelerating slip on the interface just preceding dynamic rupture, consistent with the idea that

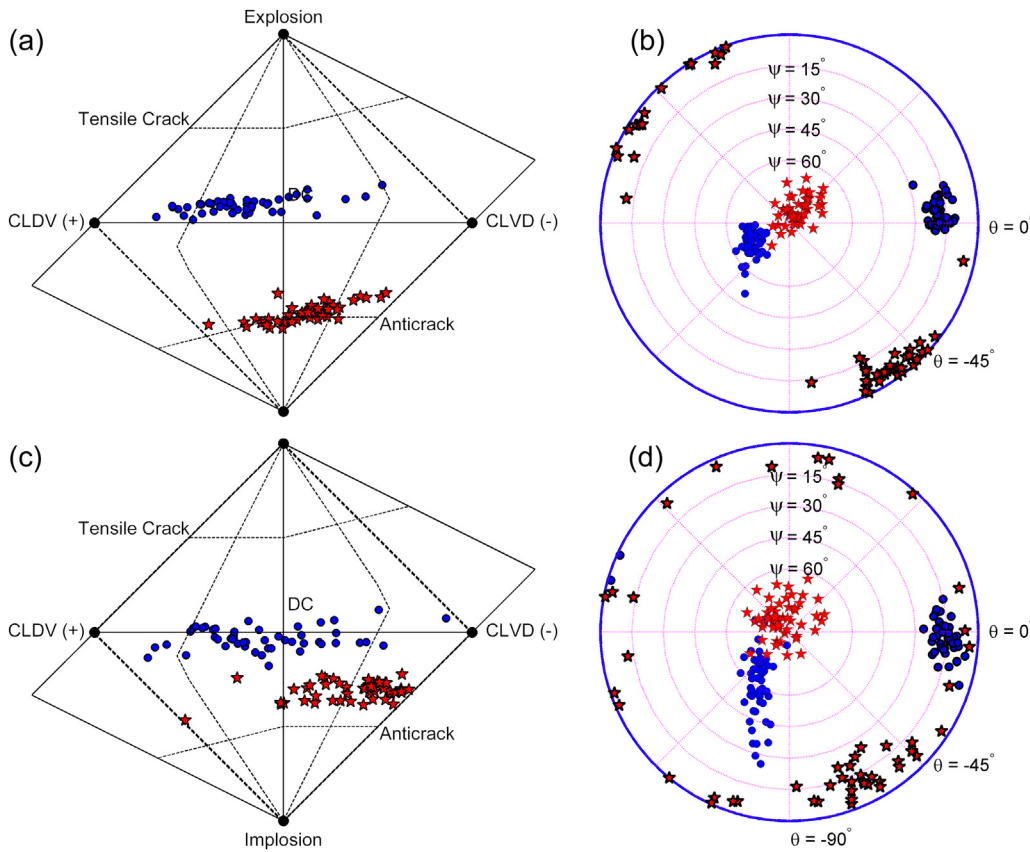


**Fig. 11.** Sensitivity analysis for MT inversion results for 4 different  $M$   $-7.1$  to  $-7.3$  AEs. In all cases shown, random errors consist of  $\pm 500$  mV uniformly distributed random errors added to each P wave amplitude estimate,  $\pm 3$  mm uniformly distributed source location error, a  $\pm 3.5$  mV uniformly distributed random error applied to one random channel's P wave amplitude estimate, and one random channel's P wave amplitude estimate removed from the inversion. Each symbol is one of 50 realizations of the MT solution performed after random errors were added to the input data. (a) and (b) show MT results for 50 realizations each of a Category 1 AE event (blue circles), and a Category 2 AE event (red stars), (c) and (d) show two different events. All AEs had RMS  $\sim 0.35$  in their initial inversion without random errors added. (For interpretation of the references to color in this figure legend, the reader is referred to the web version of this article.).

foreshocks are the byproduct of the nucleation process.

Our rough estimate of  $h^*$  is also similar to the dimensions of the coalescence of AEs during fracture of intact granite, which suggests that there may be quantitative similarities between rupture initiation on intact rocks and on preexisting faults.

## 6.2. Rock pin as an asperity

The rock pin was designed to act as an idealized asperity on the sawcut fault. Asperities are thought to be patches on the fault plane that are stronger and/or more seismogenic either due to mineralogical, rheological, or geometrical characteristics (i.e. an asperity could be a bump on the fault or composed of stronger or more unstable material). Recent earthquake simulations with heterogeneous fault properties have mainly focused on a planar fault with regions of contrasting material properties, often with differences in rate- and state-dependent friction parameters. (e.g. <sup>70–73</sup>).

Our pin of intact rock represents an end member where the asperity has the strength of intact rock of the same type as the surrounding host rock. We find that because it is only 4% of the fault area, it does not control the overall strength of the fault. For example, the peak strength before DSE2 is no higher than peak strength before subsequent DSEs after the asperity had been fractured (see Fig. 2b). Our idealized asperity also had a higher fracture energy than the sawcut fault, and this likely dominated its behavior. Though not a perfect comparison, our pin may have some similarities to a fault bend, jog, or small stepover. It initially acted as an inhibitor of dynamic rupture by stopping DSE1. Then it was loaded by creep of the sawcut fault and became seismically visible: it produced a multitude of smaller seismic events that could easily be described as foreshocks to the much larger dynamic rupture (DSE2) that followed. This process is reminiscent of swarm-like foreshocks to  $M$  5 to  $M$  7 earthquakes in California that were observed to occur near geometrical complexities.<sup>53</sup> Once the pin was sufficiently

destroyed (and fracture energy sufficiently reduced), dynamic rupture nucleated on the fault plane and swept through the geometrical complexity.

## 6.3. Implosion mechanisms within a dilative process zone

The intact granite pin was sheared by creep of the sawcut fault and formed a dilative process zone characteristic of Coulomb materials and depicted schematically in Fig. 12. Intense AE activity ( $> 2000$  Category 2 AEs) was associated with the initial destruction of the pin, but despite the overall dilatancy of the shear process zone, the AE focal mechanisms were exclusively implosive and mapped close to an anticrack on the Hudson plot. Implosive mechanisms are common in more porous rocks such as sandstones and are associated with the formation of a compaction band or shear bands (e.g. <sup>14</sup>), but these mechanisms are not expected in a low porosity crystalline rock like granite. One might expect that fracture of intact rock would include AEs with opening crack mechanisms (e.g. <sup>64</sup>), and previous studies of fracture of intact granite at 20 MPa indicated that more than 60% of recorded AEs had predominantly shear or tensile mechanisms,<sup>59</sup> but at higher confining stress (150 MPa), implosive mechanisms are more commonly observed, even in granite.<sup>65</sup> (We ruled out the possibility that our sensor polarity was inadvertently reversed by both checking raw data and using the sense of Category 1 DC mechanisms as a reference.)

Since the seismic manifestation of the pin failure was implosive, and the overall deformation was dilatancy, most of the creation of the shear process zone must have occurred aseismically. The formation of tensile cracks and wing cracks around preexisting flaws in the granite (Fig. 12a and b) occurred either too slowly to radiate AEs or produced AEs that were too small to be detected and analyzed with our system ( $M < -7.5$ ). On the other hand, compaction events—either due to brittle grain crushing, or triggered by slip over prominent and competent features in the process zone (e.g. filled arrows in Fig. 12c)—became



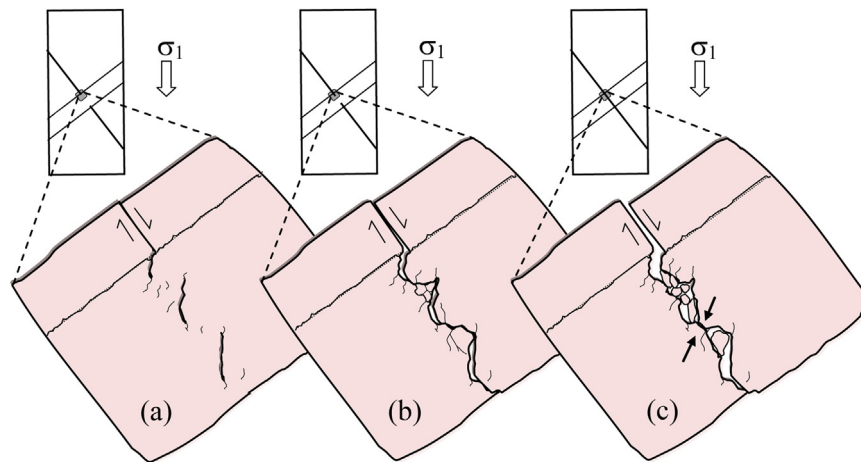


**Fig. 12.** Schematic diagram of the dilative fracture process zone at the intersection of the intact granite pin and the sawcut fault. Tensile fractures and wing cracks shown in (a) and (b) did not produce detectable AEs, but thousands of AEs with implosive mechanisms (c) were recorded.

unstable and produced the largest amplitude AEs ( $-7.5 < M < -6.0$ ). How this process leads to rotation of the azimuth of our Category 2 events (Fig. 10b) is not clear and will require further analysis.

#### 6.4. An aseismic imprint

Upon subsequent loading (DSEs 3–10, Fig. 4), no AEs were located within a 30 mm wide annulus (shadow zone) centered on the relic pin. The post-mortem pin, shown in Fig. 13, revealed a thick layer (2–4 mm) of fractured and crushed granite containing a significant portion of fine-grained material referred to as fault gouge. While intact Westerly granite has very low porosity ( $< 0.1\%$ ), the crushed and disaggregated grains that are formed during fracture (e.g. Fig. 12c) have an increased porosity of roughly 1–4%. We believe that the gouge layer within the fractured pin propped open the adjacent fault surfaces and that this was probably responsible for the lack of AE in the vicinity of the pin (Fig. 4c). A few additional AEs were detected in the area of pin, and they still exhibited exclusively implosive mechanisms, but they accounted for  $< 10\%$  of all AEs recorded after DSE2 (Fig. 4).

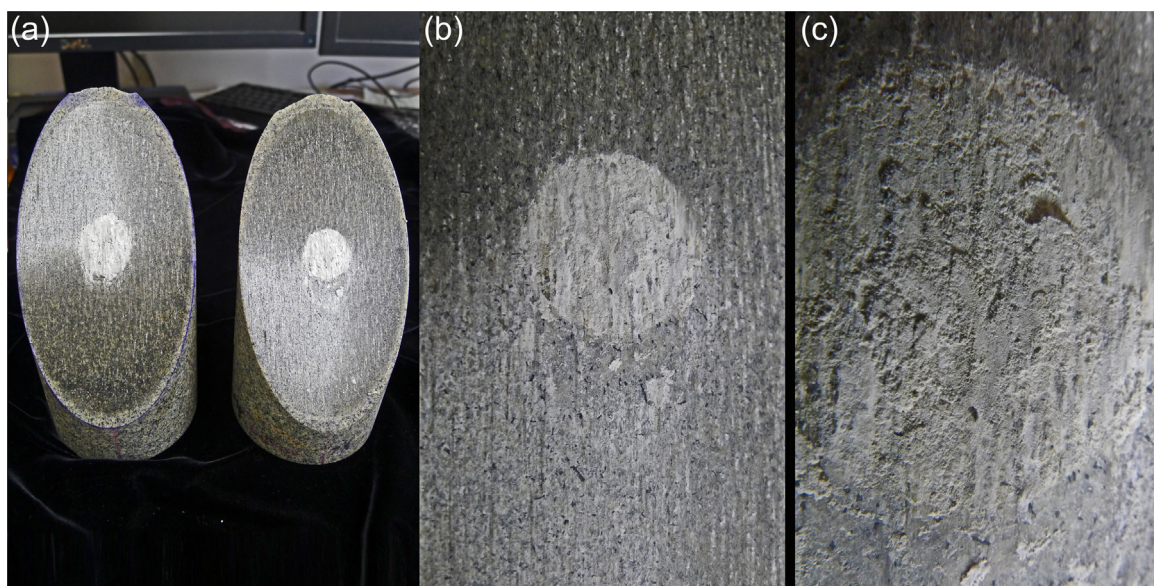
Seismic waves produced by DSEs that ruptured through the relic pin and thick gouge layer were not significantly different from those produced by DSEs on a sawcut sample without the pin,<sup>26</sup> as shown in

Fig. 5.

#### 7. Conclusions

This study explores the effects of macroscopic heterogeneity on a simulated fault in Westerly granite deformed at 80 MPa. Intended to model an asperity, our sample contained a pin of intact rock that traversed an otherwise standard sawcut fault. We presented mechanical and seismic observations of the fracture of the pin and subsequent DSEs (stick-slips). Results were compared to a previous study on an identical sawcut sample without a pin.<sup>26</sup>

The presence of the granite pin had a significant influence on deformation behavior. It apparently arrested the first, small-amplitude dynamic rupture event (DSE1), but continued aseismic creep on the sawcut transferred stress and progressively sheared the intact pin. From AE hypocenter locations, we imaged fracture fronts that migrated from the surface to the interior of the pin, and ultimately formed a zone of crushed fault gouge. The final stages of pin failure occurred in a few seconds. Creep on the fault surface accelerated and most of the  $\sim 200$  MPa shear strength drop in the pin occurred quasistatically. The full-sized DSE that followed (DSE2) was delayed until the granite pin was completely bisected. Then rupture nucleated on the sawcut surface



**Fig. 13.** Post-mortem photos of the sample and close ups of the gouge layer left behind from the sheared rock pin.

about 2 diameters away from the pin and propagated through the fractured pin. A study of the seismic waves radiated during the DSEs showed that DSE2 did not produce any anomalous seismic radiation compared to later DSEs or those generated on the sawcut fault without a pin, though a slight trend of decreasing high frequency radiation with increasing cumulative slip was observed. Following DSE2, the strength contrast of the pin was erased and subsequent DSEs occurred on the fault surface as in previously reported experiments without a pin. The only notable difference was an aseismic shadow zone around the relic pin where no AEs occurred, presumably because the newly formed fault gouge propped open the fault. The clusters of foreshocks that occurred just before and in the same location as the hypocenters of DSE3 through DSE10 had ~40 mm spatial dimensions, roughly consistent with the critical patch size  $h^*$  for dynamic slip. The coalescence of AEs just prior to the initiation of dynamic rupture in intact granite samples (observed in previous studies) also has dimensions comparable to our estimate of  $h^*$ .

We found clear differences between AEs associated with pin fracture and subsequent AEs on the sawcut fault plane in terms of timing and focal mechanism but not magnitude. AEs on the fault plane had focal mechanisms that were predominantly double couple, with orientations consistent with slip on the sawcut fault and less than 15% isotropic components. Events generated during shearing of the pin all showed significant negative isotropic components (compaction) and were located near the anticrack on the Hudson source-type plot. The orientations of these events were also distinct from those on the fault plane. The clear separation in event types allowed us to separate variability in source mechanisms from scatter due to analysis imprecision. We found the isotropic component to be a robust discriminator of event type, while variation in the percentage of CLVD versus DC was mostly due to errors associated with imprecise P wave amplitude estimates.

The formation of the shear process zone at the intersection of the sawcut fault and the intact pin produced a 2–4 mm thick gouge layer. This produced a high rate of AE, yet, remarkably, all of the AEs had significant compaction components. This leads us to believe that most of the dilative processes shown schematically in Fig. 12 were aseismic, and it demonstrates how the seismic manifestation of certain faulting processes can be unexpected.

In this laboratory experiment, we linked mechanical data such as sample average forces and displacements to seismic data from M -6 to -8 AEs and M -3 to -4 DSEs (stick-slips), in a manner that is rarely achieved in studies of larger earthquakes. While this work provided rich results at the laboratory scale, the applicability to larger natural earthquakes is not yet clear. For example, it is possible that at larger length scales negative isotropic components of MTs would be hidden behind shear mechanisms. The scaling of the aseismic “shadow” zone around the remnant asperity is also unclear. These questions might be answered by future experiments on meter-sized samples with more realistic heterogeneity.

## Acknowledgements

The authors would like to acknowledge helpful reviews by Nick Beeler, Art McGarr, and two anonymous reviewers as well as helpful discussions with Hiroki Sone and Grzegorz Kwiatak. Data used in this paper were acquired during laboratory experiments at the U.S. Geological Survey in Menlo Park, California. Data can be found in an electronic archive at <https://doi.org/10.5066/F7HM57R4>.

## References

1. Rodriguez I, Stanchits S, Burghardt J. Data-driven, in situ, relative sensor calibration based on waveform fitting moment tensor inversion. *Rock Mech Rock Eng*. 2017;50:891–911. <https://doi.org/10.1007/s00603-016-1144-4>.
2. Kwiatak G, Plenkers K, Martínez-Garzón P, Leonhardt M, Zang A, Dresen G. New insights into fracture process through in-situ acoustic emission monitoring during fatigue hydraulic fracture experiment in Äspö Hard Rock Laboratory. *Procedia Eng*.

- 2017;191:618–622.
3. Martínez-Garzón P, Kwiatak G, Sone H, Bohnhoff M, Dresen G, Hartline C. Spatiotemporal changes, faulting regimes, and source parameters of induced seismicity: a case study from The Geysers geothermal field. *J Geophys Res Solid Earth*. 2014;119:8378–8396. <https://doi.org/10.1002/2014JB011385>.
4. Kaven JO, Hickman SH, Davatzes NC. Using micro-seismicity and seismic velocities to map subsurface geologic and hydrologic structure within the coso geothermal field, California. In: *Proceedings of the 36rd Workshop on Geothermal Reservoir Engineering*. Stanford University, Stanford, California;30 January–1 February 2012, SGP-TR-194.
5. Šílený J, Milev A. Source mechanism of mining induced seismic events—resolution of double couple and non double couple models. *Tectonophysics*. 2008;456:3–15.
6. Collins DS, Pettitt WS, Young RP. High-resolution mechanics of a microearthquake sequence. *Pure Appl Geophys*. 2002;159:197–219.
7. Savage HM, Keranen KM, Schaff DP, Dieck C. Possible precursory signals in damage zone foreshocks. *Geophys Res Lett*. 2017;44:5411–5417. <https://doi.org/10.1002/2017GL073226>.
8. Imanishi K, Uchide T. Non-self-similar source property for microforeshocks of the 2014 Mw 6.2 Northern Nagano, central Japan, earthquake. *Geophys Res Lett*. 2017;44:5401–5410. <https://doi.org/10.1002/2017GL073018>.
9. Duboeuf L, De Barros L, Cappa F, Guglielmi Y, Deschamps A, Seguy S. Aseismic motions drive a sparse seismicity during fluid injections into a fractured zone in a carbonate reservoir. *J Geophys Res: Solid Earth*. 2017;122:8285–8304.
10. Brace WF, Byerlee JD. Stick-slip as a mechanism for earthquakes. *Science*. 1966;153(3739):990–992.
11. Kilgore BD, McGarr A, Beeler NM, Lockner DA. Earthquake source properties from instrumented laboratory stick-slip. In: Thomas M, Bhat H, Mitchell T, eds. *Fault Zone Dynamic Processes: Evolution of Fault Properties During Seismic Rupture*. Washington, D.C. and Hoboken: John Wiley & Sons; 2017:151–169.
12. Manthei G. Characterization of acoustic emission sources in a rock salt specimen under triaxial compression. *Bull Seismol Soc Am*. 2005;95:1674–1700. <https://doi.org/10.1785/0120040076>.
13. Zang A, Wagner FC, Stanchits S, Dresen G, Andresen R, Haidekker MA. Source analysis of acoustic emissions in Aue granite cores under symmetric and asymmetric compressive loads. *Geophys J Int*. 1998;135(3):1113–1130.
14. Kwiatak G, Charalampidou E-M, Dresen G. An improved method for seismic moment tensor inversion of acoustic emissions through assessment of sensor coupling and sensitivity to incidence angle. *Int J Rock Mech Min Sci*. 2014;65:153–161. <https://doi.org/10.1016/j.ijrmms.2013.11.005>.
15. Grosse C, Reinhardt H, Dahm T. Localization and classification of fracture types in concrete with quantitative acoustic emission measurement techniques. *NDT&E Int*. 1997;30(4):223–230.
16. Li BQ, Einstein HH. Comparison of visual and acoustic emission observations in a four point bending experiment on barre granite. *Rock Mech Rock Eng*. 2017;50(9):2277–2296.
17. McLaskey GC, Lockner DA, Kilgore BD, Beeler NM. A robust calibration technique for acoustic emission systems based on momentum transfer from a ball drop. *Bull Seismol Soc Am*. 2015;105(1):257–271.
18. Yoshimitsu N, Kawakata H, Takahashi N. Magnitude -7 level earthquakes: a new lower limit of self-similarity in seismic scaling relationships. *Geophys Res Lett*. 2014;41:4495–4502.
19. McLaskey GC, Kilgore BD, Lockner DA, Beeler NM. Laboratory generated M -6 earthquakes. *Pure Appl Geophys*. 2014;171(10):2601–2615.
20. Goodfellow SD, Young RP. A laboratory acoustic emission experiment under in situ conditions. *Geophys Res Lett*. 2014;41(10):3422–3430. <https://doi.org/10.1002/2014GL059965>.
21. Lockner D. The role of acoustic emission in the study of rock fracture. *Int J Rock Mech Min Sci Geomech Abstr*. 1993;30(7):883–899. [https://doi.org/10.1016/0148-9062\(93\)90041-B](https://doi.org/10.1016/0148-9062(93)90041-B).
22. Goebel THW, Sammis CG, Becker TW, Dresen G, Schorlemmer D. A comparison of seismicity characteristics and fault structure in stick-slip experiments and nature. *Pure Appl Geophys*. 2013;172(8):2247–2264.
23. Lockner DA, Byerlee JD. Fault growth and acoustic emissions in confined granite. *J Appl Mech Rev*. 1992;45(3):S165–S173.
24. Thompson BD, Young RP, Lockner DA. Premonitory acoustic emissions and stick-slip in natural and smooth-faulted Westerly granite. *J Geophys Res*. 2009;114:B02205. <https://doi.org/10.1029/2008JB005753>.
25. Goebel THW, Kwiatak G, Becker T, Brodsky E, Dresen G. What allows seismic event to grow big?: Insights from b-value and fault roughness analysis on laboratory stick-slip experiments. *Geology*. 2017;45(9):815–818.
26. McLaskey GC, Lockner DA. Preslip and cascade processes initiating laboratory stick-slip. *J Geophys Res Solid Earth*. 2014;119:6323–6336. <https://doi.org/10.1002/2014JB011220>.
27. Passelègue FX, Schubnel A, Nielsen S, Bhat HS, Deldicque D, Madariaga R. Dynamic rupture processes inferred from laboratory microearthquakes. *J Geophys Res Solid Earth*. 2016;121:4343–4365. <https://doi.org/10.1002/2015JB012694>.
28. Lockner DA, Okubo PG, Dieterich JH. Containment of stick-slip failures on a simulated fault by pore fluid injection. *Geophys Res Lett*. 1982;9:801–804.
29. Gephart JW, Forsyth DW. An improved method for determining the regional stress tensor using earthquake focal mechanism data: application to the San Fernando earthquake sequence. *J Geophys Res*. 1984;89:9305–9320.
30. Hardebeck JL, Michael AJ. Damped regional-scale stress inversions: methodology and examples for southern California and the Coalinga aftershock sequence. *J Geophys Res*. 2006;111:B11310. <https://doi.org/10.1029/2005JB004144>.
31. McNamara DE, Benz HM, Herrmann RB, Bergman EA, et al. Earthquake hypocenters and focal mechanisms in central Oklahoma reveal a complex system of reactivated



- subsurface strike-slip faulting. *Geophys Res Lett.* 2015;42:2742–2749. <https://doi.org/10.1002/2014GL062730>.
32. Ford SR, Dreger DS, Walter WR. Identifying isotropic events using a regional moment tensor inversion. *J Geophys Res.* 2009;114:B01306. <https://doi.org/10.1029/2008JB005743>.
  33. Julian BR, Foulger GR, Monastero FC, Bjornstad S. Imaging hydraulic fractures in a geothermal reservoir. *Geophys Res Lett.* 2010;37:L07305. <https://doi.org/10.1029/2009GL040933>.
  34. U.S. Congress, Office of Technology Assessment. Seismic Verification of Nuclear Testing Treaties, Washington, DC: U.S. Government Printing Office;1988:139.
  35. Stein S, Wysession M. *An Introduction to Seismology, Earthquakes, and Earth Structure*. Oxford: Blackwell Publishing; 2003.
  36. Stanchits SA, Lockner DA, Ponomarev AV. Anisotropic changes in P-wave velocity and attenuation during deformation and fluid infiltration of granite. *Bull Seismol Soc Am.* 2003;93(4):1803–1822.
  37. Aki K. Scaling law of seismic spectrum. *J Geophys Res.* 1967;72:1217–1231.
  38. Walter WR, Mayeda K, Gok R, Hofseter A. The scaling of seismic energy with moment: Simple models compared with observations. In: Abercrombie R, ed. Washington, D.C.: AGU; 2006:25–41. Earthquakes: Radiated Energy and the Physics of Earthquake Faulting Geophysical Monograph Series; vol. 170.
  39. McLaskey GC, Lockner DA. Calibrated acoustic emission system records m-3.5 to m-8 events generated on a saw-cut granite sample. *Rock Mech Rock Eng.* 2016;49:4527–4536.
  40. Harris F. On the use of windows for harmonic analysis with discrete Fourier transform. *Proc IEEE.* 1978;66(1):51–83.
  41. Hanks T, Kanamori H. A moment magnitude scale. *J Geophys Res.* 1979;84(B5):2348–2350.
  42. Brune JN. Tectonic stress and spectra of seismic shear waves from earthquakes. *J Geophys Res.* 1970;75:4497–5009.
  43. Summers R, Byerlee J. Summary of Results of Frictional Sliding Studies, at Confining Pressures Up to 6.98 kb, in Selected Rock Materials, U.S. Geological Survey, Open File Report 77-142;1977:129.
  44. Lockner DA, Kilgore BD, Beeler NM, Moore DE. The transition from frictional sliding to shear melting in laboratory stick-slip experiments. In: Thomas M, Bhat H, Mitchell T, eds. *Fault Zone Dynamic Processes: Evolution of Fault Properties During Seismic Rupture*. Washington, D.C. and Hoboken: John Wiley & Sons; 2017:105–130.
  45. McLaskey GC, Kilgore BD. Foreshocks during the nucleation of stick-slip instability. *J Geophys Res Solid Earth.* 2013;118:2982–2997. <https://doi.org/10.1002/jgrb.50232>.
  46. Lockner DA, Byerlee JD, Kuksenko V, Ponomarev A, Sidorin A. Quasi-static fault growth and shear fracture energy in granite. *Nature.* 1991;350:39–42.
  47. Lockner DA, Byerlee JD, Kuksenko V, Ponomarev A, Sidorin A. Observations of quasistatic fault growth from acoustic emissions. In: Evans B, Wong T-f., eds. *Fault Mechanics and Transport Properties of Rocks*. London: Academic Press; 1992:3–31.
  48. Lockner DA, Byerlee JD. Precursory AE patterns leading to rock fracture. In: Hardy HR, ed. *Proceedings of the Fifth Conference on Acoustic Emission/Microseismic Activity in Geological Structures and Materials*. Trans Tech Publications; Clausthal-Zellerfeld, Germany;1995:45–58.
  49. Thompson BD, Young RP, Lockner DA. Fracture in Westerly granite under AE feedback and constant strain rate loading: nucleation, quasi-static propagation, and the transition to unstable fracture propagation. *Pure Appl Geophys.* 2006;163:995–1019. <https://doi.org/10.1007/s00024-006-0054-x>.
  50. Moore DE, Lockner DA. The role of microcracking in shear-fracture propagation in granite. *J Struct Geol.* 1995;17:95–114.
  51. Reches Z, Lockner DA. Nucleation and growth of faults in brittle rocks. *J Geophys Res.* 1994;99(B9):18159–18173.
  52. Lockner DA, Beeler NM. Rock failure and earthquakes. In: Lee W, Kanamori H, Jennings P, Kisslinger C, eds. *International Handbook of Earthquake and Engineering Seismology, Part A*. Amsterdam: Academic Press; 2002:505–537.
  53. Dodge DA, Beroza GC, Ellsworth WL. Detailed observations of California foreshock sequences: implications for the earthquake initiation process. *J Geophys Res.* 1996;101:22371–22392.
  54. Kato A, Obara K, Igarashi T, Tsuruoka H, Nakagawa S, Hirata N. Propagation of slow slip leading up to the 2011 Mw9.0 Tohoku-Oki earthquake. *Science.* 2012;335:705–708. <https://doi.org/10.1126/science.1215141>.
  55. Yamashita F, Fukuyama E, Mizoguchi K, Takizawa S, Xu S, Kawakata H. Scale dependence of rock friction at high work rate. *Nature.* 2015;528(7581):254–257.
  56. Aki K, Richards PG. *Quantitative Seismology*. Sausalito, Calif: University Science Books; 2002.
  57. Ohtsu M. Simplified moment tensor analysis and unified decomposition of acoustic emission source: application to in situ hydrofracturing test. *J Geophys Res.* 1991;96:6211–6221.
  58. Lei X, Nishizawa O, Kusunose K, Satoh T. Fractal structure of the hypocenter distributions and focal mechanism solutions of acoustic emission in two granites of different grain sizes. *J Phys Earth.* 1992;40:617–634.
  59. Graham CC, Stanchits S, Main IG, Dresen G. Comparison of polarity and moment tensor inversion methods for source analysis of acoustic emission data. *Int J Rock Mech Min Sci.* 2010;47(1):161–169. <https://doi.org/10.1016/j.ijrmms.2009.05.002>.
  60. Rück M, Rahner R, Sone H, Dresen G. Initiation and propagation of mixed mode fractures in granite and sandstone. *Tectonophysics.* 2017;717:270–283.
  61. Kwiatek G, Martínez-Garzon P, Bohnhoff M. HybridMT: A MATLAB/shell environment package for seismic moment tensor inversion and refinement. *Seismol Res Lett.* 2016;87(4):964–976. <https://doi.org/10.1785/0220150251>.
  62. Hudson JA, Pearce RG, Rogers RM. Source type plot for inversion of moment tensor. *J Geophys Res.* 1989;94(B1):765–774.
  63. Stanchits S, Vinciguerra S, Dresen G. Ultrasonic velocities, acoustic emission characteristics and crack damage of basalt and granite. *Pure Appl Geophys.* 2006;163(5–6):975–994. <https://doi.org/10.1007/s00024-006-0059-5>.
  64. Aker E, Kühn D, Vavryčuk V, Soldal M, Oye V. Experimental investigation of acoustic emissions and their moment tensors in rock during failure. *Int J Rock Mech Min Sci.* 2014;70:286–295. <https://doi.org/10.1016/j.ijrmms.2014.05.003>.
  65. Kwiatek G, Goebel THW, Dresen G. Seismic moment tensor and b value variations over successive seismic cycles in laboratory stick-slip experiments. *Geophys Res Lett.* 2014;41:5838–5846. <https://doi.org/10.1002/2014GL060159>.
  66. Dieterich JH. Earthquake nucleation on faults with rate- and state-dependent friction. *Tectonophysics.* 1992;211:115–134.
  67. Rice JR. Spatio-temporal complexity of slip on a fault. *J Geophys Res.* 1992;98(B6):9885–9907.
  68. Rubin AM, Ampuero J-P. Earthquake nucleation on (aging) rate and state faults. *J Geophys Res.* 2005;110:B11312. <https://doi.org/10.1029/2005JB003686>.
  69. Ampuero J-P, Rubin AM. Earthquake nucleation on rate-and-state faults: aging and slip laws. *J Geophys Res.* 2008;113:B01302. <https://doi.org/10.1029/2007JB005082>.
  70. Nadeau RM, Johnson LR. Seismological studies at Parkfield VI: moment release rates and estimates of source parameters for small repeating earthquakes. *Bull Seismol Soc Am.* 1998;88(3):790–814.
  71. Beeler NM, Lockner DA, Hickman SH. A simple stick-slip and creep-slip model for repeating earthquakes and its implication for microearthquakes at Parkfield. *Bull Seismol Soc Am.* 2001;91(6):1797–1804.
  72. Ide S, Aochi H. Earthquakes as multiscale dynamic ruptures with heterogeneous fracture surface energy. *J Geophys Res.* 2005;110(B11303) <https://doi.org/10.1029/2004JB003591>.
  73. Kaneko Y, Carpenter BM, Nielsen SB. Nucleation process of magnitude 2 repeating earthquakes on the San Andreas Fault predicted by rate-and-state fault models with SAFOD drill core data. *Geophys Res Lett.* 2017;44(1):162–173. <https://doi.org/10.1002/2016GL071569>.